Arch Appl Mech (2016) 86:39–58
DOI 10.1007/s00419-015-1095-3

SPECIAL

P. N. Demmie · M. Ostoja-Starzewski

Local and nonlocal material models, spatial randomness, and impact loading

Received: 20 February 2015 / Accepted: 25 November 2015 / Published online: 31 December 2015

Abstract In many material systems, both man-made and natural, we have an incomplete knowledge of geometric or material properties, which leads to uncertainty in predicting their performance under dynamic loading. Given the uncertainty and a high degree of spatial variability in properties of geological formations subjected to impact, a stochastic theory of continuum mechanics would be useful for modeling dynamic response of such systems. In this paper, we examine spatial randomness in local and nonlocal material-mechanics models. We begin with classical linear elasticity. Then, we consider nonlocal elasticity and, finally, peridynamic theory. We discuss a formulation of stochastic peridynamic theory and illustrate this formulation with examples of impact loading of geological materials with uncorrelated versus correlated properties, sampled in a Monte Carlo sense. We examine wave propagation and damage to the material. The most salient feature is the absence of spallation, referred to as disorder toughness, which, in fact, generalizes similar results from earlier quasi-static damage mechanics.

Keywords Continuum mechanics · Nonlocal · Peridynamics · Stochastic mechanics · Random media · Impact

1 Introduction

In many systems, we have an incomplete knowledge of geometrical or material properties, which leads to uncertainty in predicting their performance under dynamic loading. Geological formations, such as shown in Fig. 1, are examples of such systems. These systems exhibit a high degree of spatial variability in their material properties. While some properties may be determined at specified locations, using wells or bore holes for geological media, estimating these properties at locations where measurements were not made entails a random error in properties. Furthermore for geological formations, the host media are discontinuous and characterized

Sandia National Laboratories is a multi-program laboratory managed and operated by Sandia Corporation, a wholly owned subsidiary of Lockheed Martin Corporation, for the U.S. Department of Energy's National Nuclear Security Administration under contract DE-AC04-94AL85000.

P. N. Demmie
Sandia National Laboratories, Albuquerque, NM 87185, USA
E-mail: pndemmi@sandia.gov

M. Ostoja-Starzewski (✉)
Department of Mechanical Science and Engineering, Institute for Condensed Matter Theory, University of Illinois at Urbana-Champaign, Urbana, IL 61801, USA
E-mail: martinos@illinois.edu

M. Ostoja-Starzewski
Beckman Institute, University of Illinois at Urbana-Champaign, Urbana, IL 61801, USA

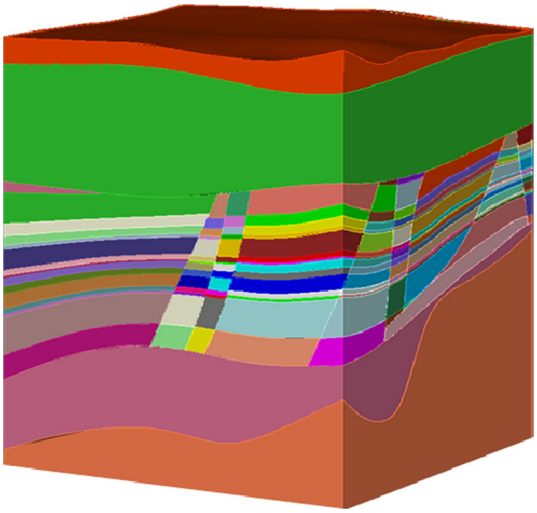

Fig. 1 Example of a randomly disordered geological formation

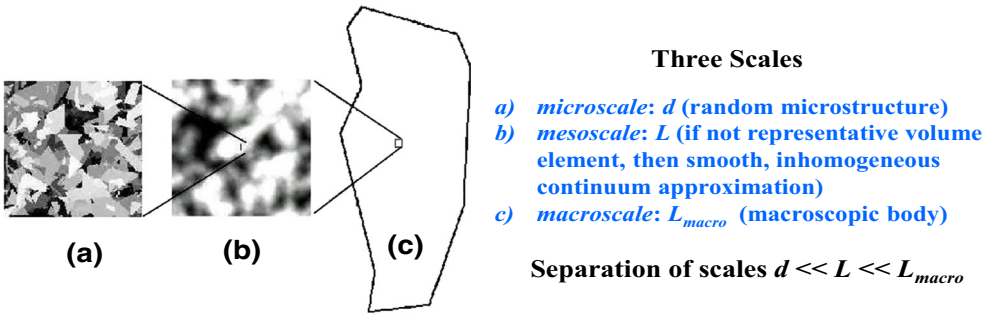

Fig. 2 Scales in random media

by highly jointed, faulted, and irregular, three-dimensional geology, as shown in Fig. 1. Discontinuity in properties leads to difficulty in predicting performance under loading, since traditional methods employ partial differential equations that are not valid at discontinuities.

A medium may be observed at various scales as shown in Fig. 2. This figure shows a medium at the microscale, mesoscale, and macroscale. In constructing a material model, a resolution level is selected. Below this level, details are not visible to the model and some enhancement to the model must be made to account, at least approximately, for these details in effective material properties. For example, if the resolution is at the macroscale, microstructural and mesostructural details are not visible. If changes in deformation field under loading are greater than the resolution level, then a conventional continuum mechanics approach is adequate. However, if such changes are below the resolution level, some enhancement to the model needs to be made to adequately capture real phenomena. Nonlocality provides such an enhancement.

Media modeled by continuum mechanics have traditionally been viewed as having properties that are well-defined local quantities with unique values at each point in space. Recognizing that systems may have complex and uncertain properties with spatial variability has prompted the development of stochastic methods to model them. One approach is to consider each property of the medium at hand as a realization of a spatially correlated random field.

Developing a nonlocal, stochastic theory of continuum mechanics would be useful in many fields of application. In this paper, we examine spatial randomness in local and nonlocal material-mechanics models. We discuss random media in Sect. 2 and modeling performance of random media in the remainder of the paper. In Sects. 3 and 4, we discuss the evolution from local gradient-based continuum formulations to nonlocal gradient-based enhancements of continuum formulations. Specifically, in Sect. 3, we consider spatial randomness in local material-mechanics models. We begin with classical linear elasticity and whether simply adopting two Lamé coefficients as random fields with smoothly inhomogeneous realizations is adequate. This approach leads us to question the admissibility of local isotropy of statistical continuum, the size of statistical volume

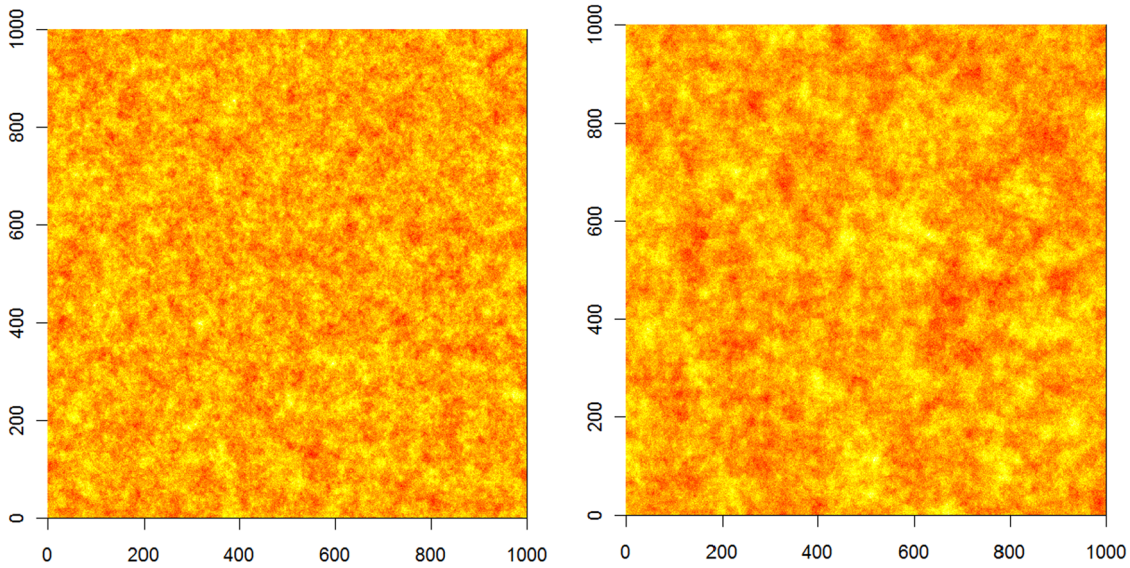

Fig. 3 Two realizations of the powered exponential random field on a 1000 × 1000 lattice

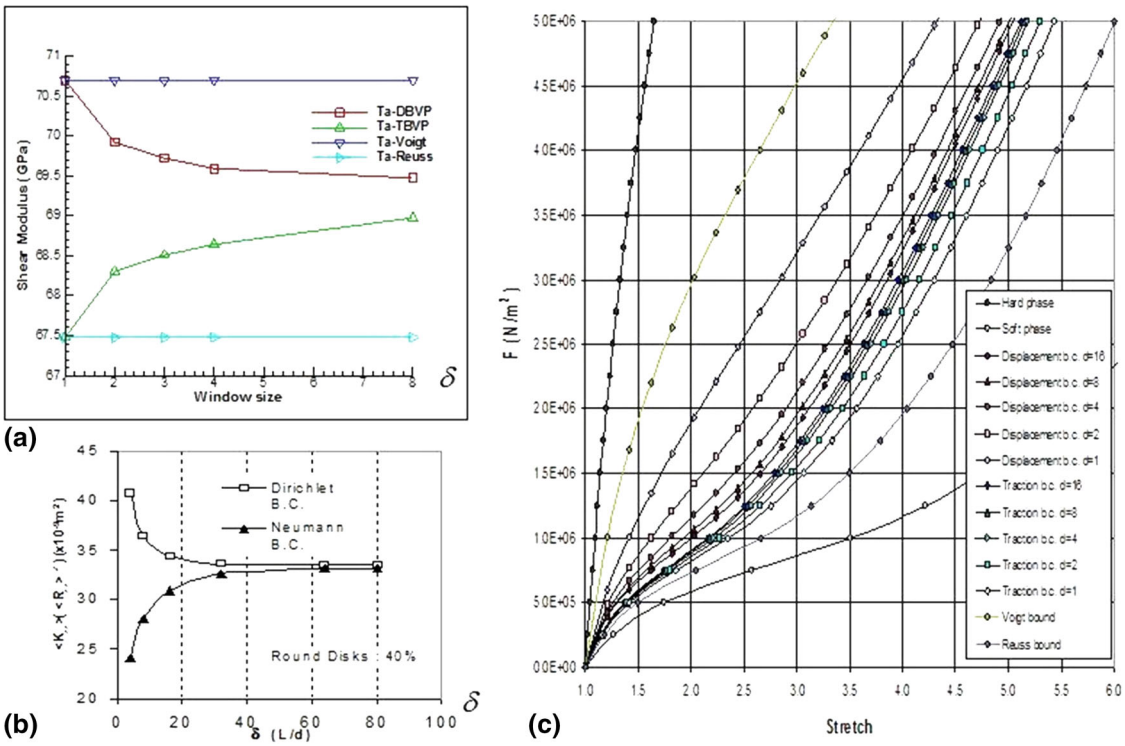

Fig. 4 **a** Effect of increasing mesoscale on the convergence of constitutive response hierarchies toward the representative volume element (RVE) in **a** linear elasticity of a random polycrystal of tantalum [9]; **b** permeability of a random porous medium [3], and **c** finite elasticity of a random composite (with neo-Hookean inclusions in an Ogden-type matrix) under uniaxial loading [3]

element, the setup of random field models of constitutive coefficients, and methods of solution of stochastic partial differential equations. Then, in Sect. 4, we consider spatial randomness in nonlocal material-mechanics models. As each of these topics is discussed, we advance from local elasticity theory, to nonlocal elasticity, and finally to peridynamic theory.

Peridynamics has become well known for its ability to grasp spatial discontinuities without ambiguous interpretations of spatial derivatives, simply because the latter are not present in the formulation. This feature,

therefore, begs the question: Why not introduce material spatial randomness? We address this issue in the setting of bond-based peridynamics. In Sect. 5, we describe a formulation of *stochastic peridynamic* theory and, in Sect. 6, we illustrate this formulation with examples of wave propagation in homogeneous and heterogeneous geological materials.

2 Random media

By a *random medium*, $\mathbf{B}$, we mean an ensemble of deterministic heterogeneous specimens (realizations), $B(\omega)$,

$$\mathbf{B} = \{B(\omega) ; \omega \in \Omega\} \tag{1}$$

Each $B(\omega)$ is parameterized by a sample event ω of the sample space, Ω. A sample space is a set equipped with a σ-algebra and a probability measure (see, e.g., [1]). Each $B(\omega)$ is a collection of scalar, vector, or tensor fields that characterize the medium called random fields.

Every $B(\omega)$ is governed by a deterministic field equation

$$\mathbf{L}(\omega, \boldsymbol{x}, t) = \mathbf{f}, \tag{2}$$

where $\mathbf{L}(\omega, \boldsymbol{x}, t)$ is a field operator, in which ω indicates the randomness, $\boldsymbol{x}$ is the position, t is the time, $\mathbf{u}$ is the displacement field, and $\mathbf{f}$ is a source or forcing function. The arguments ω and $\boldsymbol{x}$ in $\mathbf{L}$ indicate the dependence on the actual realization and location in the random medium, respectively [2,3]. Additionally, from the micromechanics standpoint, one also needs to admit the dependence of $\mathbf{L}$ on the scale of resolution [3], a so-called *mesoscale* (see Sect. 3).

In order to introduce spatial randomness of material density into material models, we usually only need scalar random fields. We work in the setting of Gaussian wide-sense stationary (WSS) isotropic fields, which are specified by assuming the mean, the standard deviation, and the normalized covariance (correlation coefficient) $\rho(x) := \mathrm{cov}\,(\mathrm{x})/Var$, where x is the norm of the vector separating any two points. From a wide range of different classes of $\rho(\boldsymbol{x})$ [4,5], in this study, we consider the *powered exponential* (or *stable*) model:

$$\rho(x) = \exp[-Ax^{\alpha}], \quad A > 0, \quad 0 < \alpha \leq 2; \tag{3}$$

Figure 3 shows sample realizations of this random field in two dimensions.

For a WSS process in one dimension, in analogy to random processes parameterized by time, one may define a *correlation length* (or *correlation radius*) as follows

$$l_{\mathrm{c}} = \int_0^{\infty} \rho(x)\mathrm{d}x. \tag{4}$$

The same concept applies to two- and three-dimensional random fields. The correlation length, l_{c} can provide the length scale in a material model when l_{c} can be chosen. Then, it specifies the mesoscale above which one may disregard any randomness (i.e., a homogeneous, deterministic continuum) or admit some weak randomness. We note that in fractal media l_{c} may be divergent.

3 Spatial randomness in local material-mechanics models

The first model one may consider is where the mass density ρ is a scalar random field

$$\mathbf{B} = \{\rho(\omega, \mathbf{x}) ; \omega \in \Omega, \mathbf{x} \in B\}, \tag{5}$$

where B is a domain occupied by the body. While in a general nonclassical continuum $\mathbf{L}$ is an integro-differential operator, let us begin with classical models, like linear elasticity, where $\mathbf{L}$ is simply a differential operator. Then, the corresponding (2) becomes

$$\left[C_{ijkl}(\omega, \mathbf{x})u_k\right]_{,jl} + b_i(\omega, \mathbf{x}) = \rho(\omega, \mathbf{x})\ddot{u}_i. \tag{6}$$

Here, besides ρ (which must not be confused with the normalized covariance of Sect. 2), we have also taken the stiffness tensor C_{ijkl} and the body force b_i to be random fields

$$\mathbf{B} = \left\{\rho(\omega, \mathbf{x}), C_{ijkl}(\omega, \mathbf{x}); \omega \in \Omega, \mathbf{x} \in B\right\}. \tag{7}$$

This leads to the field equation

$$C_{ijkl}\left(u_{k,lj}+u_{l,kj}\right)/2+C_{ijkl,j}\left(u_{k,l}+u_{l,k}\right)/2+b_i\left(\omega,\mathbf{x}\right)=\rho\left(\omega,\mathbf{x}\right)\ddot{u}_i. \tag{8}$$

A popular way to proceed further in stochastic solid mechanics is to take an isotropic Hooke's law

$$C_{ijkl}(\omega,\mathbf{x})=\lambda(\omega,\mathbf{x})\delta_{ij}\delta_{kl}+\mu(\omega,\mathbf{x})(\delta_{ik}\delta_{jl}+\delta_{il}\delta_{jk}), \tag{9}$$

which leads to two special cases:

(i) The pair (λ,μ) is piecewise constant, representing a locally heterogeneous microstructure made of a number of microdomains, so that the governing equation

$$\lambda(\omega,\mathbf{x})u_{k,ki}+\mu(\omega,\mathbf{x})(u_{j,ij}+u_{i,jj})+b_i\left(\omega,\mathbf{x}\right)=\rho\left(\omega,\mathbf{x}\right)\ddot{u}_i. \tag{10}$$

This equation is recognized to be the stochastic Navier equation; it needs to be augmented by continuity conditions at interfaces between all the contiguous microdomains.

(ii) λ and μ are of class C^1, representing a smoothly inhomogeneous material, whereby (8) becomes

$$\begin{aligned}&\lambda(\omega,\mathbf{x})u_{k,ki}+\mu(\omega,\mathbf{x})(u_{j,ij}+u_{i,jj})+\lambda(\omega,\mathbf{x})_{,i}\,u_{k,k}\\&\quad+\mu_{,l}\left(\omega,\mathbf{x}\right)u_{(i,l)}+\mu_{,k}\,u_{k,i}+b_i\left(\omega,\mathbf{x}\right)=\rho\left(\omega,\mathbf{x}\right)\ddot{u}_i.\end{aligned} \tag{11}$$

In anti-plane elasticity [say, in the x_1x_2-plane], we identify the displacement to be a scalar field $u=u_3$, so that $C_{ijkl}=C_{3j3l}$ is effectively a second-rank tensor C_{jl}, and (11) simplifies to

$$\left(C_{jl}(\omega,\mathbf{x})u_{,l}\right)_{,j}=C_{jl}(\omega,\mathbf{x})u_{,lj}+C_{jl}(\omega,\mathbf{x})_{,j}\,u_{,l}+b_i\left(\omega,\mathbf{x}\right)=\rho\left(\omega,\mathbf{x}\right)\ddot{u}. \tag{12}$$

If the material is locally isotropic, $C_{jl}=C\delta_{jl}$ and we have

$$\left(C(\omega,\mathbf{x})u_{,j}\right)_{,j}=C(\omega,\mathbf{x})u_{,jj}+C(\omega,\mathbf{x})_{,j}\,u_{,j}+b_i\left(\omega,\mathbf{x}\right)=\rho\left(\omega,\mathbf{x}\right)\ddot{u}, \tag{13}$$

which is a stochastic hyperbolic partial differential equation in two dimensions, effectively resulting in a Laplacian term plus a scalar product of gradient of stiffness multiplied with the gradient of u. In the absence of the inertia term, this becomes the basic stochastic elliptic partial differential equation.

In the very special case when C = constant, which corresponds to spatial inhomogeneity of mass density only, and considering the frequency space setting while neglecting the body forces, one arrives at the stochastic Helmholtz equation [3]:

$$\nabla^2u+k_0^2n^2(\omega,\mathbf{x})u=0. \tag{14}$$

Approximate analytical solutions for the first moment $\langle\mathbf{u}\rangle$ (i.e., the true average solution) and, eventually, the second moment $\langle\mathbf{u^2}\rangle$ are possible in situations of wave lengths being either much larger or smaller than the typical heterogeneity size [6]. In general, there is no sufficiently developed mathematics for differential equations with arbitrary inhomogeneous coefficients.

The above discussion indicates that, in all the cases, there are two key considerations. First, we consider the typical length scale of the initial-boundary-value problem relative to the typical size of the heterogeneity. Now, suppose we simply carry out a straightforward averaging of the random fields of material properties to get

$$\langle\mathbb{L}\rangle\,\hat{\mathbf{u}}=\mathbf{f}, \tag{15}$$

and then find the true average solution $\langle\mathbf{u}\rangle$ of the stochastic problem (2) governed by an equation [2–4]

$$\left\langle\mathbb{L}^{-1}\right\rangle^{-1}\langle\mathbf{u}\rangle=\mathbf{f}. \tag{16}$$

Then, we consider the question "What is the difference between $\langle\hat{\mathbf{u}}\rangle$ and $\langle\mathbf{u}\rangle$?" To make progress, one needs to consider (i) the underlying microstructure from which the spatial randomness stems, (ii) other continuum models, and (iii) how such models may be solved. Note (16) has been obtained by first inverting (2) to find $\mathbf{u}=\mathbb{L}^{-1}\left(\omega,\mathbf{x},t\right)\mathbf{f}$, then ensemble averaging to get $\langle\mathbf{u}\rangle=\langle\mathbb{L}^{-1}\left(\omega,\mathbf{x},t\right)\rangle\mathbf{f}$, and then inverting once again.

The key role in accounting for randomness is the mesoscale $\delta=L/d$, where L is the actual spatial resolution and d the typical microstructural size (e.g., one grain) (Fig. 2a). The mesoscale (i.e., scale-dependent)

homogenization can be conducted in a systematic way from the standpoint of the Hill-Mandel homogenization condition which requires the equivalence of energetic and mechanical interpretations of energy stored in the material domain [7,8]:

$$\overline{\boldsymbol{\sigma} : \boldsymbol{\varepsilon}} = \overline{\boldsymbol{\sigma}} : \overline{\boldsymbol{\varepsilon}} \Leftrightarrow \overline{\boldsymbol{\sigma}' : \boldsymbol{\varepsilon}'} = 0 \Leftrightarrow \int_{\partial B_\delta} (\mathbf{t} - \overline{\boldsymbol{\sigma}} \cdot \mathbf{n}) \cdot (\mathbf{u} - \overline{\boldsymbol{\varepsilon}} \cdot \mathbf{x}) \mathrm{d}S = 0. \tag{17}$$

This condition leads to three possible boundary conditions:

(i) uniform displacement (Dirichlet):

$$\mathbf{u}(\mathbf{x}) = \boldsymbol{\varepsilon}^0 \cdot \mathbf{x} \quad \forall \mathbf{x} \in \partial B_\delta; \tag{18}$$

(ii) uniform traction (Neumann):

$$\mathbf{t}(\mathbf{x}) = \boldsymbol{\sigma}^0 \cdot \mathbf{n} \quad \forall \mathbf{x} \in \partial B_\delta; \tag{19}$$

(iii) mixed orthogonal:

$$\left\lfloor \mathbf{t}(\mathbf{x}) - \boldsymbol{\sigma}^0 \cdot \mathbf{n} \right\rfloor \cdot \left\lfloor \mathbf{u}(\mathbf{x}) - \boldsymbol{\varepsilon}^0 \cdot \mathbf{x} \right\rfloor = 0 \quad \forall \mathbf{x} \in \partial B_\delta. \tag{20}$$

Each of these conditions results in a different mesoscale response.

With increasing mesoscale δ, we obtain scale-dependent bounds on the elastic response of the aggregate by setting up and solving boundary-value problems consistent with (15) and (16), respectively. Thus, at any point $\mathbf{x}$ and at any mesoscale δ, two estimates of (actually, bounds on) effective properties may be introduced: $\boldsymbol{C}_\delta^d$ and $\boldsymbol{C}_\delta^t = \left(\boldsymbol{S}_\delta^t\right)^{-1}$, where d or t denote, respectively, displacement-controlled (traction-controlled) boundary conditions applied to the mesoscale. Consequently, given the choice of a mesoscale δ, there are two bounding tensor-valued random fields:

$$\mathbf{C}_\delta^d : \Omega \times \mathbf{R}^2 \to \mathbf{R}^3 \qquad \mathbf{S}_\delta^t : \Omega \times \mathbf{R}^2 \to \mathbf{R}^3. \tag{21}$$

While Fig. 2b shows one realization of an inhomogeneous continuum at the mesoscale (b), in reality, there are two continuum approximations depending on whether we think of $\boldsymbol{C}_\delta^d$ or $\boldsymbol{C}_\delta^t$. These two mesoscale random fields are continuous-valued with continuous parameter $\mathbf{x} \in \mathbf{R}^2$.

The random composite material $\mathbf{B}$ is now described (actually bounded) by two sets of realizations: $\{\boldsymbol{C}_\delta^d(\omega, \mathbf{x}); \omega \in \Omega, \mathbf{x} \in \mathbf{R}^2\}$ and $\{\boldsymbol{S}_\delta^t(\omega, \mathbf{x}); \omega \in \Omega, \mathbf{x} \in \mathbf{R}^2\}$ (See Fig. 8.1 in [3]).

These approximations, as they directly depend on the choice of δ, provide two alternate inputs to the field equation governing the global response on the smoothing mesoscale δ

$$\left[C_{ij}(\omega, \mathbf{x}) T_{,j}\right]_i = 0. \tag{22}$$

Note that, besides $\mathbf{C}^{\mathrm{d}}$ and $\mathbf{S}^{\mathrm{t}}$, we can define the mesoscale response via uniform orthogonal mixed boundary conditions, denoted by dt. As a result, we have three different approximating random fields

$$\mathbf{B}^d = \{B(\omega); \omega \in \Omega\}, \qquad \mathbf{B}^t = \{B(\omega); \omega \in \Omega\}, \qquad \mathbf{B}^{dt} = \{B(\omega); \omega \in \Omega\}, \tag{23}$$

with $\boldsymbol{C}_\delta^{dt}$ having no bounding property. It follows that there is no unique way of setting up a mesoscale random field. Many examples of scaling (i.e., scale dependence) of $\boldsymbol{C}_\delta^d$ and $\boldsymbol{S}_\delta^t$ are found in [3,10], and one is reproduced here in Fig. 4a. Indeed, constitutive responses of a wide range of random materials of (non) linear elastic, inelastic, permeable, and even coupled field type have been studied within this framework.

One way to determine the macroscale response is to use the fields $\boldsymbol{C}_\delta^d$ and $\boldsymbol{S}_\delta^t$ to set up two stochastic finite-element methods based, respectively, on the minimum potential and complementary energy principles so as to obtain micromechanically informed bounds on the macroscopic response, even for high-contrast materials [11]. While such a study was conducted, so far, in anti-plane linear elastostatics, here we are interested in elastodynamics with the likely presence of fracture and damage.

4 Spatial randomness in nonlocal material-mechanics models

Following [12,13], consider linear elastostatics on the random field of a fourth-rank stiffness tensor $C_{ijkl} = \{C_{ijkl}(\omega, \mathbf{x}); \omega \in \Omega, \mathbf{x} \in \mathbf{R}^2\}$. Then, the equations governing the ensemble average (deterministic) fields of the random medium are nonlocal in nature

$$\begin{aligned} \langle \sigma_{ij}(\mathbf{x}) \rangle_{,j} &= 0 \\ \langle \sigma_{ij}(\mathbf{x}) \rangle &= \int_{\mathbf{B}} \bigwedge_{ijkl} (\mathbf{x}, \mathbf{x}') \langle \varepsilon_{kl}(\mathbf{x}') \rangle \, \mathrm{d}\mathbf{x}' \\ \langle \varepsilon_{kl} \rangle &= \left(\langle u_{k,l} \rangle + \langle u_{l,k} \rangle \right) / 2. \end{aligned} \tag{24}$$

Here we employ σ_{ij} and ε_{kl} to denote symmetric Cauchy stress and strain tensors. In (21), $\Lambda_{ijkl}(\mathbf{x}, \mathbf{x}')$ is an infinite sum of integro-differential operators, involving moments of all orders of the random field C_{ijkl}

$$\Lambda_{ijkl}(\mathbf{x}, \mathbf{x}') = \lfloor \langle C_{ijkl} \rangle + D_{ijkl}(\mathbf{x}') \rfloor \, \delta(\mathbf{x} - \mathbf{x}') + E_{ijkl}(\mathbf{x}, \mathbf{x}'), \tag{25}$$

where $D_{ijkl}(\mathbf{x}')$ and $E_{ijkl}(\mathbf{x}, \mathbf{x}')$ are functions of the statistical properties of C_{ijkl} and the free-space Green's function of the nonstatistical problem. Addition of a deterministic body force field f_i does not change the results. When the fluctuations in C_{ijkl} are small, $D_{ijkl}(\mathbf{x}')$ and $E_{ijkl}(\mathbf{x}, \mathbf{x}')$ may be evaluated explicitly, and this was done by Beran and McCoy [12,13] in the special case of the realizations $C_{ijkl}(\omega)$ being locally isotropic, i.e., expressed in terms of a vector random field of two Lamé coefficients $\{[\lambda(\omega, \mathbf{x}), \mu(\omega, \mathbf{x})]; \omega \in \Omega, \mathbf{x} \in \mathbf{R}^2\}$.

Next, considering this random field to be statistically homogeneous and mean ergodic, one may disregard the contributions of this operator for $|\mathbf{x} - \mathbf{x}'| > l_c$ (the correlation length). Thus, since only the neighborhood within the distance l_c of $\mathbf{x}$ has a significant input into the integral (21), one may expand $\langle \varepsilon_{kl}(\mathbf{x}') \rangle$ in a power series about $\mathbf{x}$

$$\begin{aligned} \langle \varepsilon_{kl}(\mathbf{x}') \rangle = \langle \varepsilon_{kl}(\mathbf{x}) \rangle &+ (x'_m - x_m) \langle \varepsilon_{kl}(\mathbf{x}) \rangle_{,m} \\ &+ \frac{(x'_m - x_m)(x'_n - x_n)}{2} \langle \varepsilon_{kl}(\mathbf{x}) \rangle_{,mn} \cdots \end{aligned} \tag{26}$$

to obtain

$$\begin{aligned} \langle \sigma_{ij}(\mathbf{x}) \rangle = &\int_{\mathbf{B}} \bigwedge_{ijkl} (\mathbf{x}, \mathbf{x}') \, \mathrm{d}\mathbf{x}' \langle \varepsilon_{kl}(\mathbf{x}) \rangle \\ &+ \int_{\mathbf{B}} \bigwedge_{ijkl} (\mathbf{x}, \mathbf{x}') (x'_m - x_m) \, \mathrm{d}\mathbf{x}' \langle \varepsilon_{kl}(\mathbf{x}) \rangle_{,m} + \cdots \end{aligned} \tag{27}$$

This expression, in turn, can be rewritten as a sum of local, plus first gradient, plus higher gradient strain effects

$$\langle \sigma_{ij} \rangle = C^*_{ijkl} \langle \varepsilon_{kl} \rangle + D^*_{ijklm} \langle \varepsilon_{kl} \rangle_{,m} + E^*_{ijklmn} \langle \varepsilon_{kl} \rangle_{,mn} + \cdots \tag{28}$$

Thus, first integral over $\mathbf{B}$ in (27) is recognized as the *effective stiffness*, C^*_{ijkl}, indeed the stiffness of a single realization $B(\omega)$ of the random material $\mathbf{B}$. If one is given the ensemble $\mathbf{B}$ of $B(\omega)$, then one may determine the microstructural statistics and hence the higher-order approximations D^*_{ijklm}, E^*_{ijklmn}, etc. In order to implement this approach, one has to admit tensor random fields, a challenging issue which we avoid here by turning to the peridynamics model which involves scalar random fields and, incidentally, also allows one to handle fracture/damage phenomena.

This section and the preceding section show what can be done with traditional treatment of mechanics of random media. We now proceed to discuss another approach to the mechanics of random media, stochastic peridynamic theory.

5 Stochastic peridynamic theory

Peridynamic theory [14] is a theory of continuum mechanics that uses integro-differential equations rather than partial differential equations containing spatial derivatives. Therefore, the equations of peridynamic theory apply at discontinuities.

A medium may be observed at various scales. In constructing a material model, a resolution level is selected. Below this level, details are not visible to the model and some enhancement to the model must be made to adequately capture, at least approximately, real phenomena. Nonlocality provides such an enhancement. Peridynamic theory is a nonlocal formulation of continuum mechanics.

Peridynamics also provides a consistent treatment of both material deformation and failure, unlike the formulations discussed in Sects. 3 and 4 which include spatial derivatives and where something special must be done to deal with the formation and evolution of cracks. Peridynamics provides a capability to predict the spontaneous formation of cracks and their subsequent growth. With peridynamics, cracks initiate and grow spontaneously as a consequence of the governing and constitutive model, and there is no need for externally supplied laws or for specifying the locations of cracks. Thus, with peridynamics, cracks are part of the solution and not part of the problem. Peridynamic theory has been used to solve problems involving loading of structures [15].

Media modeled by continuum mechanics, including peridynamic theory, are typically viewed as having properties that are well-defined local quantities with unique values at each point in space. However, in many systems, we do not have a complete knowledge of geometrical or material properties, which leads to uncertainty in predicting their performance under dynamic loading. Recognizing that systems may have complex and uncertain properties with spatial variability has prompted the development of stochastic methods to model them.

Therefore,

(1) peridynamics provides nonlocality;
(2) peridynamics provides a consistent treatment of deformation and failure of a medium; and
(3) stochastic peridynamics further provides the capability to address spatial variability or lack of complete knowledge of properties of the medium.

In Sect. 5.1, we provide a brief review of peridynamic theory and in Sect. 5.2 we discuss formulating stochastic peridynamic theory. In Sect. 5.3, we describe the peridynamic materials used for the examples of wave propagation in geological media that we consider in Sect. 6, where each property of this media as a realization of a spatially correlated random field.

5.1 Peridynamic theory

The version of peridynamic theory introduced in 2000 is called bond-based peridynamics [14]. A more general version, state-based peridynamics, was introduced later [16]. In this paper, we only consider bond-based peridynamics.

Figure 5 depicts a peridynamic body that occupies a domain $\boldsymbol{R}$.

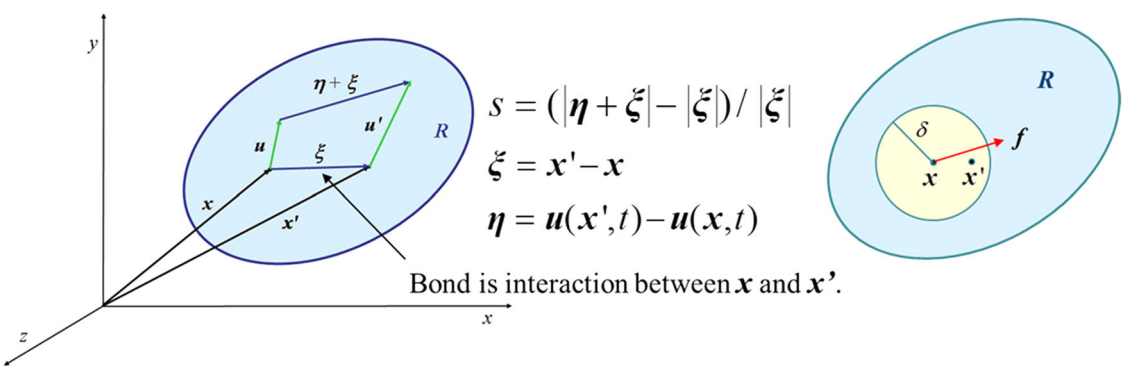

Fig. 5 A peridynamic body occupying a domain $\boldsymbol{R}$ (bond-based PD)

In Fig. 5 (left), $\boldsymbol{\xi}$ is the relative position between points $\boldsymbol{x}$ and $\boldsymbol{x}'$ in the reference configuration and $\boldsymbol{\eta}$ is the difference in displacements at these points. Then, $(\boldsymbol{\eta}+\boldsymbol{\xi})$ is the relative position of the points originally at $\boldsymbol{x}, \boldsymbol{x}'$ in the deformed configuration. The scalar quantity s in this figure is called the stretch and is a measure of relative deformation. Figure 5 (right) shows a sphere $S_\delta(\boldsymbol{x}) = \{\boldsymbol{x}' : |\boldsymbol{x}' - \boldsymbol{x}| < \delta\}$ of radius δ centered at the point $\boldsymbol{x}$. It is assumed that there is a distance δ, called the *horizon*, such that the peridynamic interaction vanishes outside $S_\delta(\boldsymbol{x})$ for each point $\boldsymbol{x}$ in the domain of analysis.

The force density at $\boldsymbol{x}$ at time t in bond-based peridynamics is given by

$$\rho(\boldsymbol{x})\,\frac{d^2}{dt^2}\,\boldsymbol{u}(\boldsymbol{x},t) = \iiint_{\boldsymbol{R}} \boldsymbol{f}(\boldsymbol{u}(\boldsymbol{x}',t)-\boldsymbol{u}(\boldsymbol{x},t),\boldsymbol{x}'-\boldsymbol{x})dV' + \boldsymbol{b}(\boldsymbol{x},t) \tag{29}$$

where $\boldsymbol{x}$ and $\boldsymbol{x}'$ are points in the reference configuration, t is the time, $\rho(\boldsymbol{x})$ is the density at $\boldsymbol{x}$, $\boldsymbol{u}$ is the displacement vector, $\boldsymbol{R}$ is the domain of the body, $\boldsymbol{f}$ is the pairwise force function (PFF), and $\boldsymbol{b}$ is the body force density.[1] The integral in (29) is a taken over the volume occupied by $\boldsymbol{R}$. Equation (29) is the fundamental equation of bond-based peridynamic theory. It is based on Newton's second law or motion for all points within the domain of analysis and does not contain any spatial derivatives. The PFF gives the force per unit volume squared at $\boldsymbol{x}$ due to material at $\boldsymbol{x}'$. It is assumed to be Riemann integrable. All constitutive properties of a material in bond-based PD are given by specifying the PFF.

5.2 Formulating stochastic peridynamic theory

In the case of random media, (29) must be generalized to *stochastic peridynamics*. This generalization means that the governing equations hold for each and every heterogeneous specimen $B(\omega)$ from the ensemble $\mathbf{B}$. In order to find the solution, one may consider two basic strategies.

Strategy 1. *Seek the stochastic response*. Each realization $B(\omega)$ of the ensemble $\mathbf{B}$ follows (29) for a specific heterogeneous material body. Hence, the response is governed for each realization $B(\omega)$ by

$$\rho(\boldsymbol{x},\omega)\,\frac{d^2}{dt^2}\,\boldsymbol{u}(\boldsymbol{x},t) = \iiint_{B(\omega)} \boldsymbol{f}(\boldsymbol{\eta},\boldsymbol{\xi},\omega)dV' + \boldsymbol{b}(\boldsymbol{x},t,\omega) \tag{30}$$

The quantities $\rho(\boldsymbol{x},\boldsymbol{\omega}), \boldsymbol{f}(\boldsymbol{\eta},\xi,\omega)$, and $\boldsymbol{b}(\boldsymbol{x},t,\omega)$ are random fields. Since there is no analytical procedure to solve this equation, even in one dimension and even for homogeneous (i.e., spatially constant) material properties, the techniques of random integral equations can hardly be applied, and the only way to proceed is in a Monte Carlo sense. A set of simulations will then give the scatter and allow one to assess an average response, and, possibly, one or two higher moments.

Strategy 2. *Seek the average response*. Upon ensemble averaging of (29) over Ω (denoted by $\langle\cdot\rangle$), the mean response of $\mathbf{B}$ is governed by

$$\langle\rho(\boldsymbol{x})\,\frac{d^2}{dt^2}\,\boldsymbol{u}(\boldsymbol{x},t)\rangle = \iiint_{\mathbf{B}} \langle\boldsymbol{f}(\boldsymbol{\eta},\boldsymbol{\xi})\rangle dV' + \langle\boldsymbol{b}(\boldsymbol{x},t)\rangle \tag{31}$$

Here, we exploited the commutativity of ensemble averaging with volume integration. The quantities $\rho(\boldsymbol{x},)$ and $\mathrm{d}^2\boldsymbol{u}(\boldsymbol{x},t)/\mathrm{d}t^2$ are cross-correlated in an unknown way. This equation is different from what would be obtained by a straightforward (naïve) averaging of spatially random material properties inherent in the random functions $\rho(\boldsymbol{x},\omega)$ and $\boldsymbol{f}(\boldsymbol{\eta},\boldsymbol{\xi},\omega)$, i.e.,

$$\hat{\rho}(\boldsymbol{x})\,\frac{d^2}{dt^2}\,\hat{\boldsymbol{u}}(\boldsymbol{x},t) = \iiint_{\mathbf{B}} \hat{\boldsymbol{f}}(\boldsymbol{\eta},\boldsymbol{\xi})dV' + \hat{\boldsymbol{b}}(\boldsymbol{x},t) \tag{32}$$

With reference to Sect. 3, the hat denotes quantities evaluated from such averages. The latter are used (without a hat) in conventional, deterministic peridynamics.

In this strategy, the basic question that arises is: How different is $\langle\boldsymbol{f}(\boldsymbol{\eta},\boldsymbol{\xi})\rangle$ computed by ensemble averaging from $\hat{\boldsymbol{f}}(\boldsymbol{\eta},\boldsymbol{\xi})$ computed by straightforward averaging? Obviously, this difference leads to a discrepancy between

[1] In (29) and elsewhere, bold quantities are vectors unless stated otherwise.

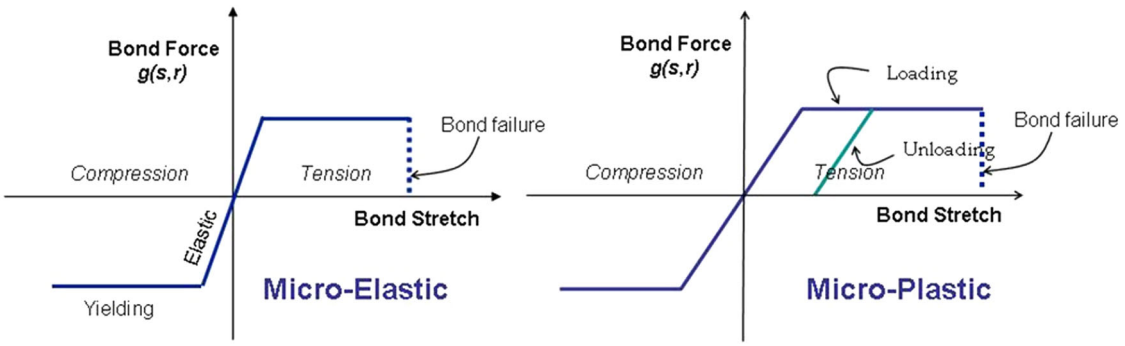

Fig. 6 Bond force for proportional, microelastic (plastic) materials

predictions of (31) and (32). Clearly, the only quantitative way to assess that difference is by pursuing both strategies separately. In general, the solution, $\langle \boldsymbol{u} \rangle$, given according to (31), has to be contrasted with the solution $\hat{\boldsymbol{u}}$ that would be obtained by a straightforward averaging approach according to (32). However, it is seen that the Strategy 2 is fundamentally incorrect and yields the first moment of response only.

In Sect. 6, we discuss several examples of wave propagation in geological media that follow Strategy 1.

5.3 Microelastic (plastic) materials in stochastic peridynamic theory

The specialization on the PFF that we will adopt for the simulation examples in Sect. 6 is a further development of the notion that points in a continuum may be considered to be connected by springs. We consider materials with a PFF having its magnitude proportional to the stretch s defined in Fig. 5. Such materials are called *proportional*, *microelastic* (*plastic*) materials.

The most general form of the PFF for proportional, microelastic (plastic) materials is

$$\boldsymbol{f}(\boldsymbol{\eta}, \boldsymbol{\xi}) = \frac{g(s, r)}{p} (\boldsymbol{\eta} + \boldsymbol{\xi}) \tag{33}$$

where g is a piecewise linear function of the stretch s, r is the magnitude of the vector $\boldsymbol{\xi}$, and p is the magnitude of the vector $\boldsymbol{\eta} + \boldsymbol{\xi}$ [14]. The function g is called the *bond force* between two points for a proportional, microelastic (plastic), peridynamic material.

Figure 6 shows the bond force dependence on bond stretch for such materials. This figure shows that the behavior of microelastic and microplastic materials differs only on unloading. A microelastic material unloads reversibly back to zero stretch, while a microplastic material that is stretched beyond the elastic limit will retain some stretch when unloaded. This figure shows a linear dependence with nonzero slope in the elastic regime and constant bond force when the yield strength magnitude is exceeded in tension or compression. This figure also indicates bond failure at some value of bond stretch. Peridynamic materials fail irreversibly when the stretch exceeds a value, s_c, called the *critical stretch*.

In numerical implementations of bond-based peridynamics, repulsive short-range forces act when points are sufficiently close. These forces prevent bonds from compressing indefinitely and violating nonimpenetrability of matter.

Figure 7 summarizes our formulation of stochastic peridynamic theory for proportional, microelastic (plastic) materials used for the examples in Sect. 6.

This figure shows the fundamental field equation under Strategy 1, (30), for a single realization, ω. For convenience, we will not consider the source term here. There is uncertainty and spatial variability in the density, ρ, and the PFF, $\boldsymbol{f}$. Thus, randomness enters through random fields for the density and PFF. For a proportional, microelastic (plastic) material with PFF given by (33), the PFF depends only on the bulk modulus, K, and the yield strength, Y. Randomness in failure enters through a random field for the critical stretch, s_c. Hence, the random medium, $\mathbf{B}$, is characterized by a collection of realizations, $B(\omega)$, consisting of random fields for material properties shown in Fig. 8—density, bulk modulus, yield strength, and critical stretch. $B(\omega)$ would also include a source term for each realization if a source were present.

This approach to stochastic peridynamics is based on the fact that variability in material property is not completely known even though one can obtain information on material properties through measurements on

- **Field equation:** $\rho(\boldsymbol{x},\omega)\,\frac{d^2}{dt^2}\boldsymbol{u}(\boldsymbol{x},t) = \iiint_R \boldsymbol{f}(\boldsymbol{\eta},\boldsymbol{\xi},\omega)\,dV'$
- **Randomness enters through the random fields:**

  density $\rho(x,\omega), \omega\ \varepsilon\ \Omega$ (sample space)

  pairwise force function $\boldsymbol{f}(\boldsymbol{\eta},\boldsymbol{\xi},\omega)$ which for proportional micro-elastic or micro-plastic materials depends on bulk modulus $K(\boldsymbol{x},\omega)$ and yield strength $Y(\boldsymbol{x},\omega)$

  critical stretch $s_0(\boldsymbol{x},\omega)$ (maximum value of stretch s)
- **Thus, the random medium B is characterized by:**

$$\mathbf{B} = \{\rho(\boldsymbol{x},\omega), K(\boldsymbol{x},\omega), Y(\boldsymbol{x},\omega), s_0(\boldsymbol{x},\omega) : \boldsymbol{x}\ \varepsilon\ \mathrm{E}^3, \omega\ \varepsilon\ \Omega\}$$

Fig. 7 Formulating stochastic peridynamic theory for microelastic (plastic) materials

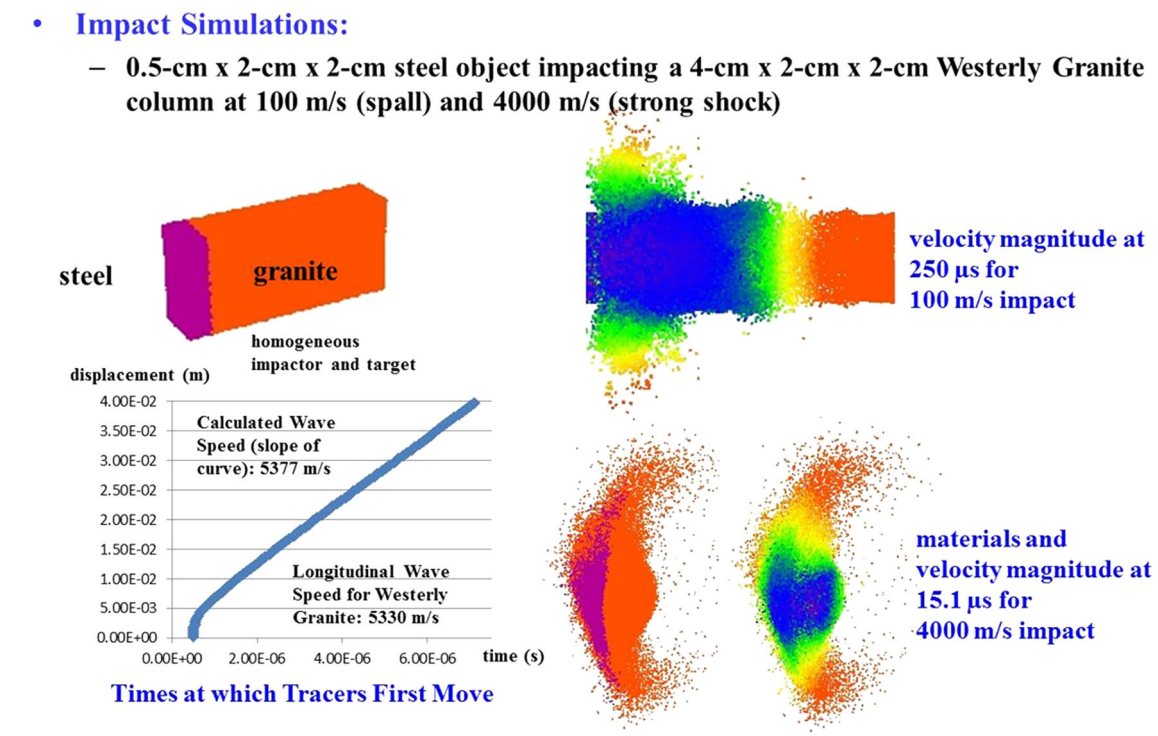

Fig. 8 Wave propagation in granite

heterogeneous media, such as geological formations. This approach is a physically realistic approach. One solves the stochastic field equation for multiple realizations and takes the average to find the mean response $\langle \boldsymbol{u} \rangle$.

6 Wave propagation in geological materials

We performed simulations to examine wave propagation in a geological material and illustrate the formulation of stochastic peridynamics described in Sect. 5.3 under Strategy 1. In this section, we will compare longitudinal wave speeds and predicted velocity distributions between homogeneous and heterogeneous materials.

Figure 8 shows the general setup for impact simulations of a 0.5 cm × 2 cm × 2 cm steel object impacting a 4 cm × 2 cm × 2 cm column of a homogeneous, isotropic material with bulk properties of Westerly Granite. We considered impact speeds of 100 and 4000 m/s. The material-property inputs for bond-based peridynamics

Table 1 Material properties for initial simulations

Material	Density (kg/m^3)	Bulk sound speed (m/s)	Yield strength (MPa)	Critical stretch (−)
Steel	7850	3212	750	0.11
Granite	2627	3750	9.8	0.000256

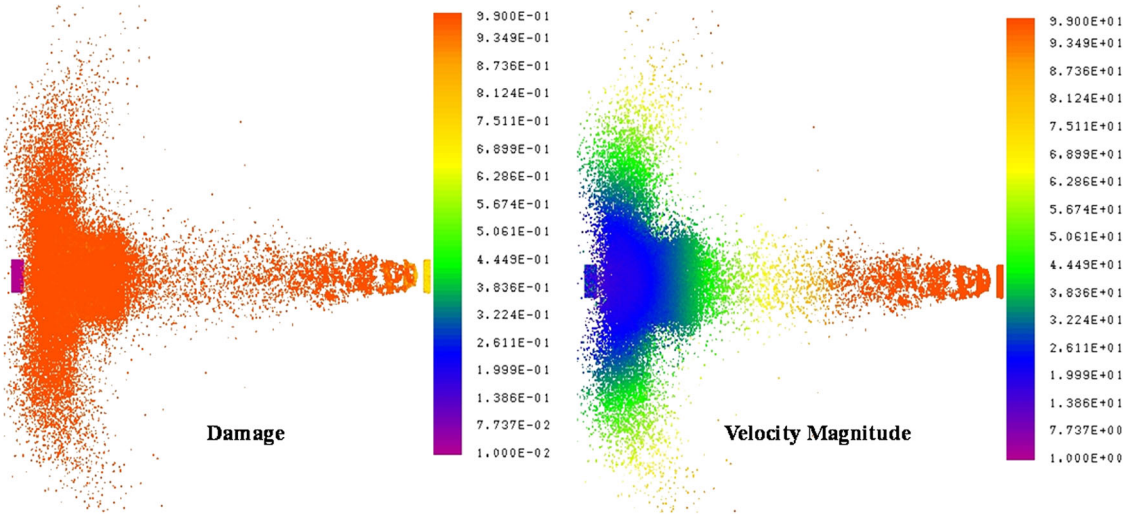

Fig. 9 Damage and velocity magnitudes at 1876 μs in 100-m/s impact

are density, bulk sound speed (square root of the bulk modulus divided by the density), yield strength, and critical stretch. Table 1 lists the material properties used for these simulations. For each simulation, the mesh spacing was 0.5 mm and the horizon was the conventional three times the mesh spacing.

The impacts produce waves that propagate through the granite. This figure also illustrates the procedure to calculate wave speed and results from two simulations for homogeneous materials. The procedure for determining wave speed is to place tracer particles (tracers) along the center line of the granite column in the direction of the impact velocity. The tracers are Lagrangian, and the position and velocity of each tracer are obtained as a function of time during a simulation. The times after impact at which each of these tracers first moves are plotted as shown in the graphic at the lower left of Fig. 8. The slope of this line after the initial rise is the wave speed. The initial behavior is due to the time that it takes for the nodes in the impactor to interact with nodes in the granite via short-range forces since at time zero they are a grid spacing apart for a uniform grid. For the homogeneous granite, this graphic shows a calculated wave speed of 5434 m/s which is in excellent agreement with the longitudinal wave speed of 5.33 km/s.

The longitudinal wave speed in Westerly granite is 5.33 km/s. At 100 m/s, the shock speed is 2241 m/s [17]. Since the shock speed for a 100 m/s impact is less than the longitudinal wave speed, the shock is not a strong shock. For the shock to be a strong shock, its speed must exceed the longitudinal wave speed. We considered an impact speed of 4000 m/s to produce a strong shock since the shock speed for an impact at 4000 m/s is 6866 m/s [17]. The shock becomes strong for impacts somewhere between 3500 and 4000 m/s.

The graphics at the right of Fig. 8 show velocity magnitudes for the 100 m/s impact simulation at 250 μs and velocity magnitudes and materials for the 4000 m/s impact simulation. at 15.1 μs. The qualitative behaviors are quite different. The beginnings of spall of the end of the granite column is evident in the graphic for the 100 m/s Impact.

Figure 9 shows damage and velocity magnitude later in the 100- m/s simulation. The graphics in this figure at 1876 μs indicate that spalling occurs in this simulation as would be expected from the speed distribution shown in Fig. 8 for this impact. Spalling does not occur during the 4000-m/s impact in the direction of the impact. Rather material is ejected at high speeds in directions nearly perpendicular to the direction of the impact. In Sect. 6.3, we show that the behavior predicted in the 4000-m/s simulation is not due to time-step instability. Features shown in these simulations are the clear prediction of material ejection and the propagation of shock waves without using artificial viscosity or other techniques to smear the shock. No special methods

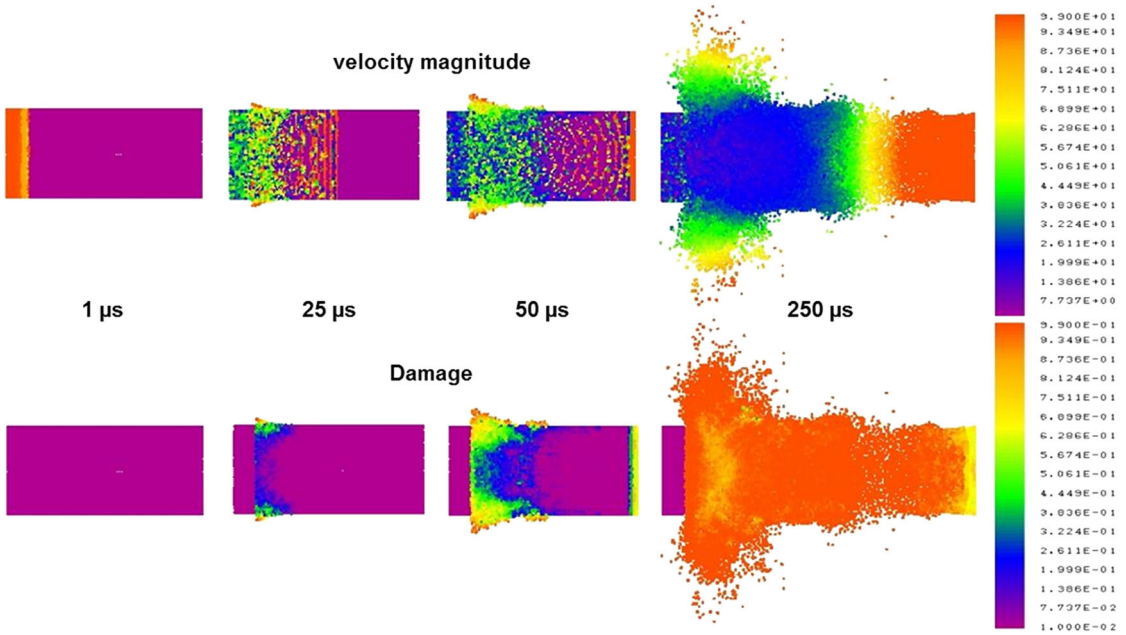

Fig. 10 Velocity magnitudes and damage during 100-m/s impact

were required to predict shock propagation or spall. The lack of need of special methods to deal with these phenomena is attributed to the nonlocality of peridynamic theory and its treatment of failure.

Figure 10 shows velocity magnitude and damage during the simulation of impact of steel into granite at 100 m/s. The velocities in the top row of this figure illustrate wave propagation resulting from the impact, and the damage distributions in the bottom row illustrate damage progression. The velocity graphics at 1 and 25 μs show wave propagation between these times. At 25 μs, material ejection transverse to the direction of impact is evident for the velocities and damage. The velocity graphics show the deceleration of the impactor as the color changes from orange to blue. Prior to 50 μs, the wave was reflected off the right boundary. By this time, the material at the right begins moving at about 100 m/s, whereas material in the interior is moving more slowly. The velocity and damage graphics at 50 μs show the initial stages of material spall in the direction of impact. As seen in Fig. 9, by 1876 μs, a section of material has broken away as indicated by the orange and adjacent yellow in the velocity graphic and the high damage in the damage graphic as indicated by the orange.

In Sects. 6.1 and 6.2, we consider heterogeneous materials with some material properties specified by random fields. In Sect. 6.1, we consider uncorrelated random fields for bulk modulus and critical stretch and, in Sect. 6.2, we consider a correlated random field for density.

6.1 Heterogeneous materials (uncorrelated random fields)

Figure 11 shows the heterogeneities that we considered. In the following examples, we choose the values for the Weibull parameters so that the mean bulk modulus and critical stretch are the same as their values for the homogeneous case.

Table 2 and Fig. 12 summarize results for the 100-m/s impact simulations. Table 2 shows wave speeds for all cases, except the jointed granite column, and Fig. 12 shows material node speeds (velocity magnitudes) for these cases.

This table shows that the calculated wave speed for the homogeneous granite (5334 m/s) agrees extremely well with the measured longitudinal wave speed in Westerly granite (5.33 km/s) for a 100- m/s impact [17]. Except for the cases of significant heterogeneity in the bulk modulus (Weibull with shape parameter $m = 0.5$), the calculated wave speeds are within 2 % of this value, with the biggest difference in these cases being the perturbed node locations.

Although variations in critical stretch do not affect the wave speeds, they do result in some differences in the highest speeds (orange) for the homogeneous and large variation in critical stretch ($m = 0.5$) cases. The

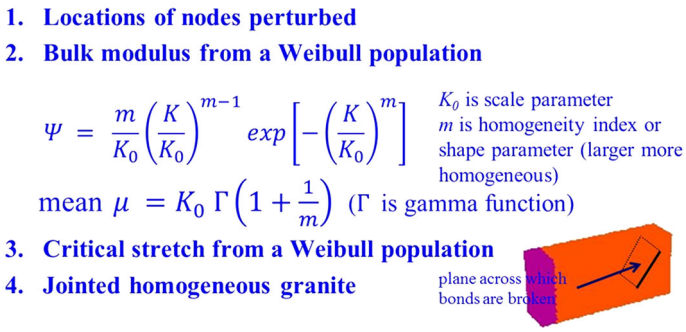

Fig. 11 Heterogeneous material simulations

Table 2 Wave speeds for 100 m/s impact

Heterogeneity	Bulk modulus m	Critical stretch m	Wave speed (m/s)
Homogeneous	–	–	5334
Node locations	–	–	5431
Weibull K	0.5	–	3371
Weibull K	50	–	5317
Weibull s_0	–	0.5	5334
Weibull s_0	–	50	5334
Weibull K and s_0	0.5	0.5	3371
Joint (oblique)*	–	–	5334
Joint (oblique)**	–	–	–

orange sections at the right indicate spallation of material from the column. From the legend in this figure, the spalled material is leaving at speeds in excess of 99 m/s, whereas most of the material is traveling at between 20 and 30 m/s.

Figure 12 shows speed distributions that are nearly identical for the homogeneous and the larger variation in bulk modulus ($m = 50$) cases. The most salient feature from comparing the cases shown in Fig. 12 is the absence of spallation at the right sides of the columns for cases where the node locations are perturbed or there is large variation ($m = 0.5$) in the bulk modulus. We refer to this feature as disorder toughness and indicate the cases in the figure showing disorder toughness. Disorder toughness generalizes similar results from quasi-static damage mechanics [3,18–20].

In the cases of large variation in bulk modulus ($m = 0.5$), there are sections of material moving at speeds 40 to 50 m/s, whereas the bulk of the column is moving at speeds between about 20 and 30 m/s. However, the high-speed spallation (orange) is not present at the right ends. Ejection speeds of material along the sides (top and bottom of graphics) are quite a bit greater in these cases than in the homogeneous case.

We also considered joints in the homogeneous granite column. Figure 12 shows material node speeds for 0- and 1.53-mm cracks. A 0-mm crack is a planar surface across which bonds are broken initially. For the 0-mm crack, damage along the crack is not 100 % since nodes on a side of the crack are still connected to nodes on the same side, whereas, for the 1.53-mm crack, damage within the crack is 100 % since the horizon is less than 1.53 mm. The material ejection patterns are quite different in these cases. In the 0-mm case, there is spallation like the homogeneous case although the shape of the spall section differs somewhat. The 0-mm crack case does not exhibit the curvature of the homogeneous case and shows an almost linear profile with a deviation from vertical that is not nearly the 45° of the crack. In contrast, the 1.53-mm case shows most ejection of material is in the direction of the 45° crack. In this case, there is no spallation at the right end of the column.

Table 3 and Fig. 13 summarize results for the 4000- m/s impact simulations. Table 3 shows wave speeds for all cases, except the jointed granite column, and Fig. 13 shows material node speeds (velocity magnitudes) for these cases. Table 3 shows that the calculated wave speed for the homogeneous granite (6866 m/s) agrees extremely well with the shock speed in Westerly granite (6866 m/s) for a 4000-m/s impact [17].

The shock speed in Westerly granite, U_p, is given by the linear Hugoniot

$$U_\mathrm{p} = 2.10\frac{\mathrm{km}}{\mathrm{s}} + 1.63u_\mathrm{p} \tag{34}$$

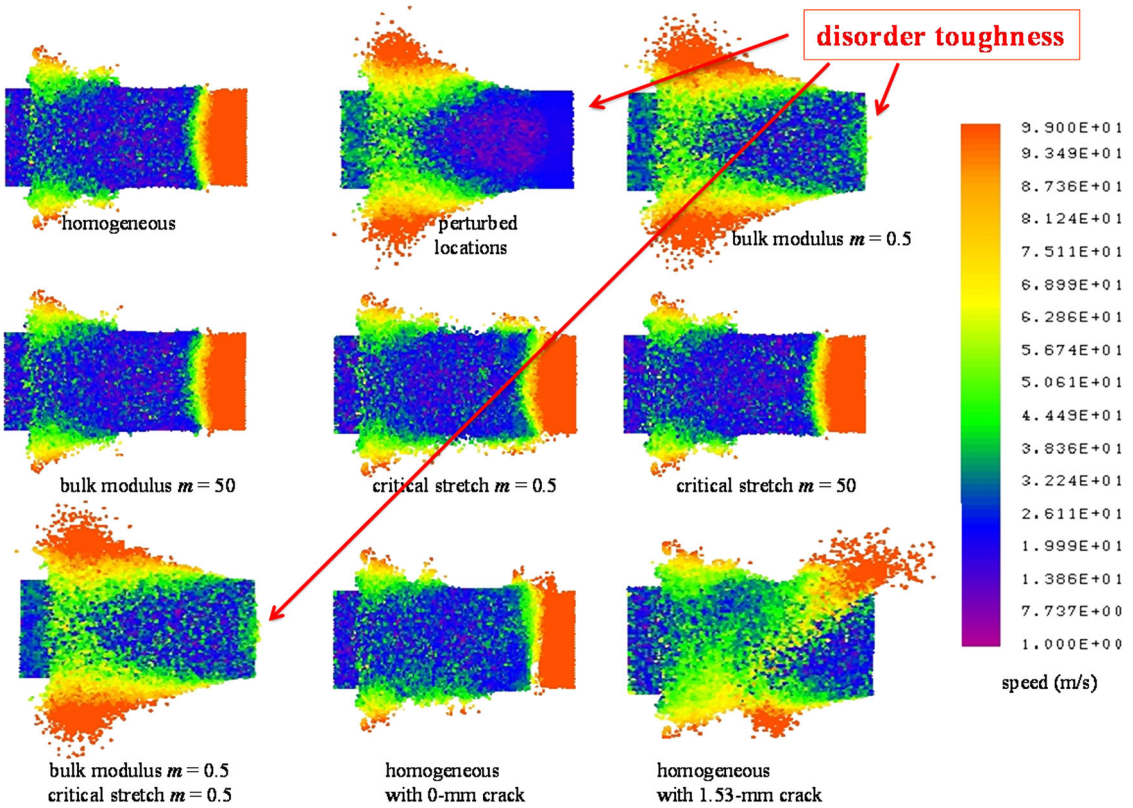

Fig. 12 Speed distributions in materials at 100 μs for 100 m/s impact

Table 3 Waves speeds for 4000 m/s impact

Heterogeneity	Bulk modulus m	Critical stretch m	Wave speed (m/s)
Homogeneous	–	–	6866
Node Locations	–	–	6707
Weibull K	0.5	–	6330
Weibull K	50	–	6937
Weibull s_0	–	0.5	6910
Weibull s_0	–	50	6910
Weibull K and s_0	0.5	0.5	6275

where u_p is the particle speed at the shock interface in km/s [17]. This speed is not the impact speed, but is calculated from the Rankine–Hugoniot jump equations [21]. For materials with the same shock impedance, the particle speed is half the impact speed. For 4340 steel impacting Westerly granite at 4000 m/s, which is the present case, the particle speed is about 2924 m/s. For a 100-m/s impact, as considered previously, the particle speed is about 86.5 m/s and the shock speed from (34) is about 2241 m/s.

In contrast to the 37 % difference in wave speeds for the 100 m/s impacts into homogeneous and heterogeneous granite, Table 3 shows that the variation in calculated wave speed for the 4000 m/s impacts is only about 9 % with the lowest speed of about 6225 m/s for Weibull with $m = 0.5$ for both bulk modulus and critical stretch. The information in this table suggests that variations in wave speed diminish as the impact speed increases and are practically nonexistent for strong shocks.

The most salient feature of the cases shown in Fig. 13 is the uniformity of the speed distributions for a 4000 m/s impact in contrast to the variation seen with heterogeneity for the 100 m/s impact shown in Fig. 12. We have no explanation for the short, vertical orange lines in Fig. 12. They are likely caused by the plotting program.

As was the case with wave speed, the information in Table 3 suggests that variations in material-speed distribution diminish as the impact speed increases and are practically nonexistent for strong shocks. For

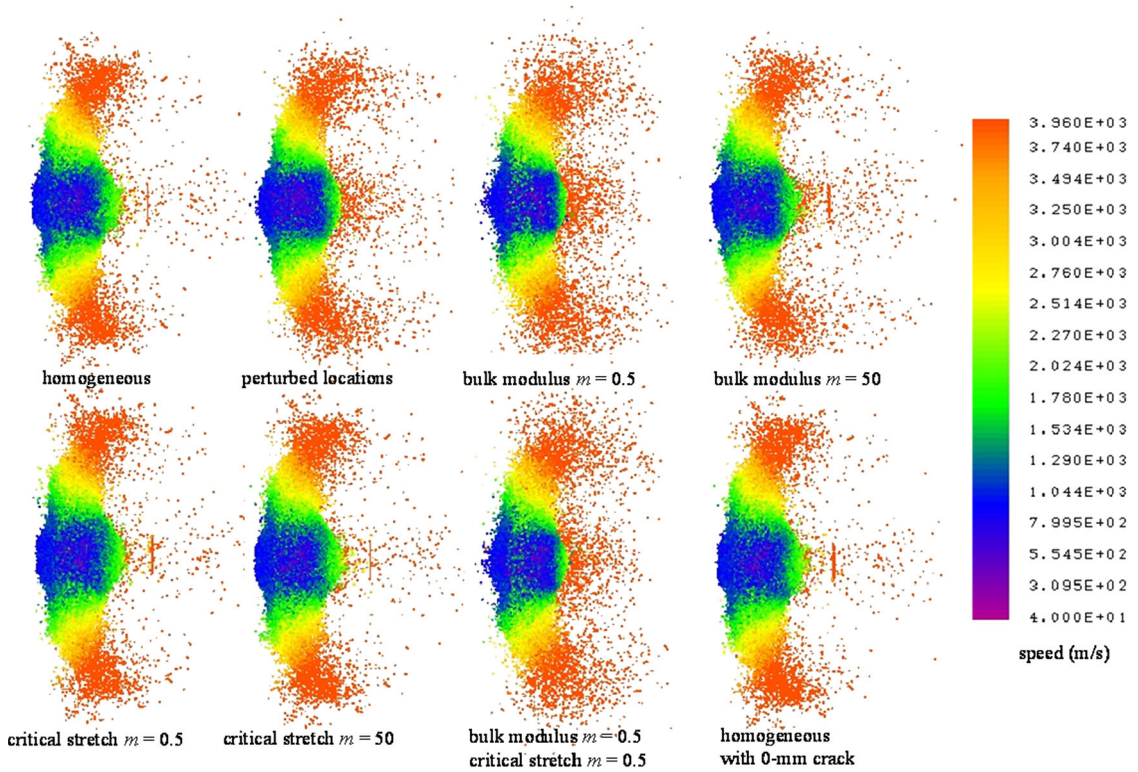

Fig. 13 Speed distributions in materials at 15 μs for 4000 m/s impact

the 4000-m/s impacts, the highest speed material ejected from the granite column is in a direction nearly perpendicular to the direction of motion. For the 100-m/s impacts, there is significant ejection in this direction only for the cases with heterogeneities that show disorder toughness.

6.2 Heterogeneous materials (correlated random fields)

In reality, material properties can be spatially correlated and material-property fields having spatial correlation must be considered. We can create different random field models depending on the assumed correlation structure and probability distribution. Then, we can examine the response of the material domain to the same impact conditions in each model and make comparisons of the reference homogeneous medium case (zero noise) with random field models (white noise and nonwhite noise) using different spatial correlations. We considered a spatially correlated random field for granite density and performed four impact simulations to examine the effects of density variation given by a spatially correlated random field.

Figure 14 shows the density distributions for the granite columns that we considered. This figure shows a homogeneous density medium with density 2627 kg/m^3 and three density random fields—correlated Gaussian random variates (RVs), these correlated RVs reduced by a factor of 1000, and uncorrelated Gaussian RVs. The RVs were generated using the open-source statistical package called R [22].

Figure 14 states the range of densities for the four cases considered. No legend is present in this figure, but the colors range from yellow for the minimum listed below the graphic to blue for the maximum listed, with green being the mean (2627 kg/m^3). The largest density variation occurs for the correlated Gaussian RVs. This case also shows the most clumping of mass. There is less clumping of mass in the uncorrelated Gaussian RV case. Although the graphic with these RVs reduced by 1000 looks variegated, there is only a 4 kg/m^3 variation in density.

Table 4 and Fig. 15 summarize results from the 100- m/s simulation.

Table 4 lists the calculated wave speeds, and Fig. 15 shows material-speed distributions at 100 μs. Table 4 shows that the calculated wave speeds for the 100 m/s impact differ by about 3 % from the wave speed in homogeneous granite (5333 m/s). As expected, the homogeneous and RV/1000 cases have nearly the same

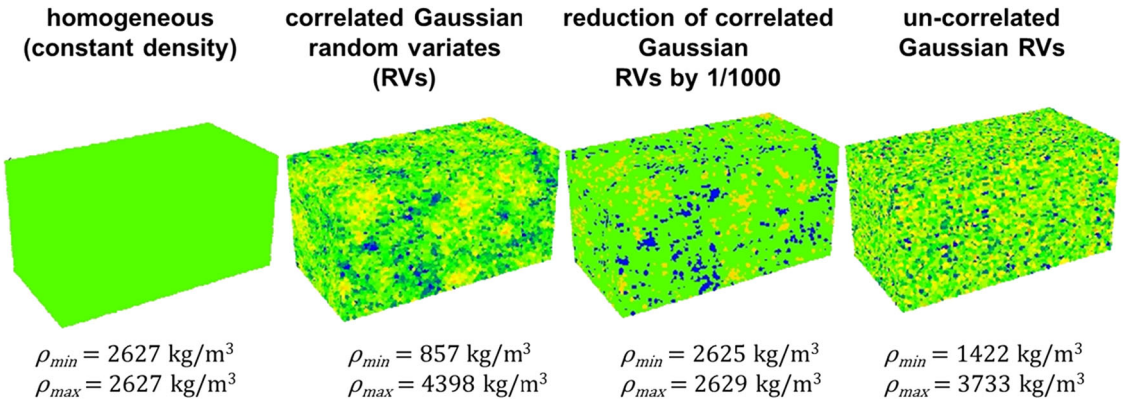

Fig. 14 Density random field

Table 4 Wave speeds for 100 m/s impact (density random field)

Case	Average density (kg/m^3)	SD (kg/m^3)	Wave speed (m/s)
Homogeneous	2627	–	5333
Correlated	2627	262.7	5198
Correlated (RV7/1000)	2627	262.7	5377
Uncorrected	2627	262.7	5269

Longitudinal wave speed for Westerly granite is 5.33 km/s. Shock-wave speed for 100 m/s impact of steel into Westerly granite is 2241 m/s. Therefore, not in strong shock regime

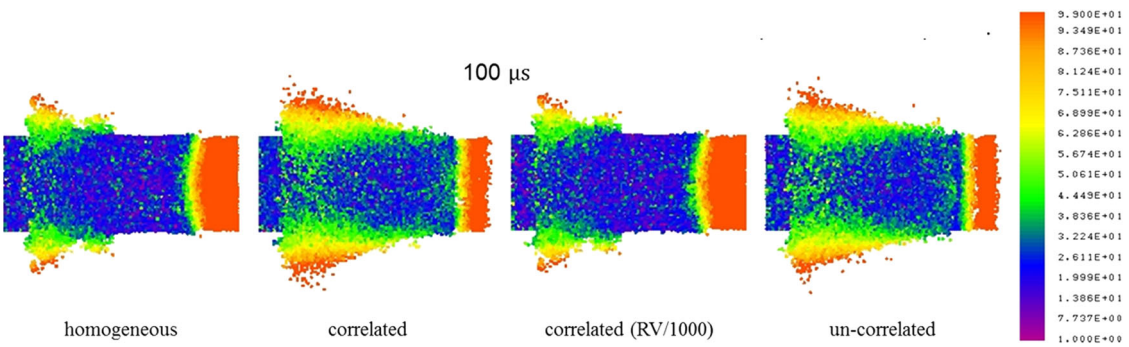

Fig. 15 Material speeds for 100 m/s impact with density random field

wave speeds. Figure 15 shows nearly identical material-speed distributions, and spallation at the right end of the column. Although the correlated and uncorrelated Gaussian cases also show spallation, the boundary between the high-speed ejection (orange) is straight rather than curved as in the homogeneous case. Also, in these cases, there is significantly more ejection from the top and bottom of the column, and the region of high velocity at the end of the column is much smaller.

Table 5 and Fig. 16 summarize results from the 4000 m/s simulation. Table 5 lists the calculated wave speeds, and Fig. 16 shows material-speed distributions at 15 μs.

Table 5 shows that the calculated wave speeds differ by about 10 % from the shock-wave speed in Westerly granite (6866 m/s). This difference is about the same as the difference for the heterogeneous media cases considered in Sect. 6.1.

The material-speed distributions in Fig. 16 are nearly identical as was the case for the heterogeneous media cases considered in Sect. 6.1. This observation supports the conjecture that variations in wave speeds and material-speed distributions diminish as the impact speed increases and are practically nonexistent for strong shocks.

Table 5 Wave speeds for 4000 m/s impact (density random field)

Case	Average density (kg/m^3)	SD (kg/m^3)	Wave speed (m/s)
Homogeneous	2627	–	6866
Correlated	2627	262.7	6340
Correlated (RV/1000)	2627	262.7	6973
Uncorrelated	2627	262.7	7050

Shock-wave speed for 4000 m/s impact of steel into Westerly granite is 6866 m/s. Obtained from linear Hugoniot $U_{\text{shock}} = 2.10$ km/s $+ 1.63\, u_{\text{particle}}$ (U and u velocities)

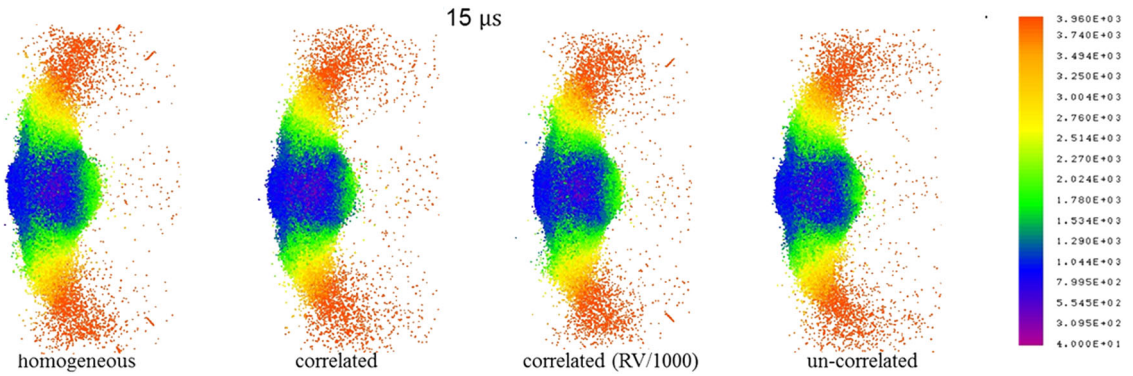

Fig. 16 Material speeds for 4000 m/s impact with density random field

6.3 On time-step stability

In this section, we address time-step stability. The Kraken computer code [23] was used for the simulations. Kraken has time-step control based on a stability analysis for (29) in one dimension using a linearized pairwise force function [24]. The code employs a safety factor to account for possible nonlinear material response that would make the estimated stable time step based on a one-dimensional analysis too large. A safety factor of S multiplies the estimated time step by S to obtain the time step used for the present computational cycle. The default safety factor is 0.8. For the simulations performed for demonstrating stochastic peridynamics, we used a safety factor of 0.1, not for stability, but to better show the propagation of waves.

To establish that the results, in particular for the 4000-m/s impact, do not result from time-step instability, we performed simulations of impacts of steel into homogeneous granite at 100 and 4000 m/s using various safety factors. Figures 17 and 18 show results from these simulations.

For the 100-m/s impact, we performed a simulation using a safety factor of 0.01, and for the 4000-m/s impact, we performed simulations using a safety factor of 0.01 and 0.001. Figure 17 shows velocity magnitudes at 250 μs for the 100-m/s impact using safety factors of 0.1 and 0.01. This figure shows no significant difference in the velocity magnitudes for the two time steps used in the simulations. Figure 18 shows velocity magnitudes at about 15 μs for the 4000-m/s impact using safety factors of 0.1, 0.01, and 0.001. This figure shows no significant differences in the velocity magnitudes for the three times steps used in the simulations.

Clearly, there is no evidence of time-step stability in these simulations. Therefore, we conclude from this examination of convergence that the predicted fragmentation phenomena do not result from time-step instability.

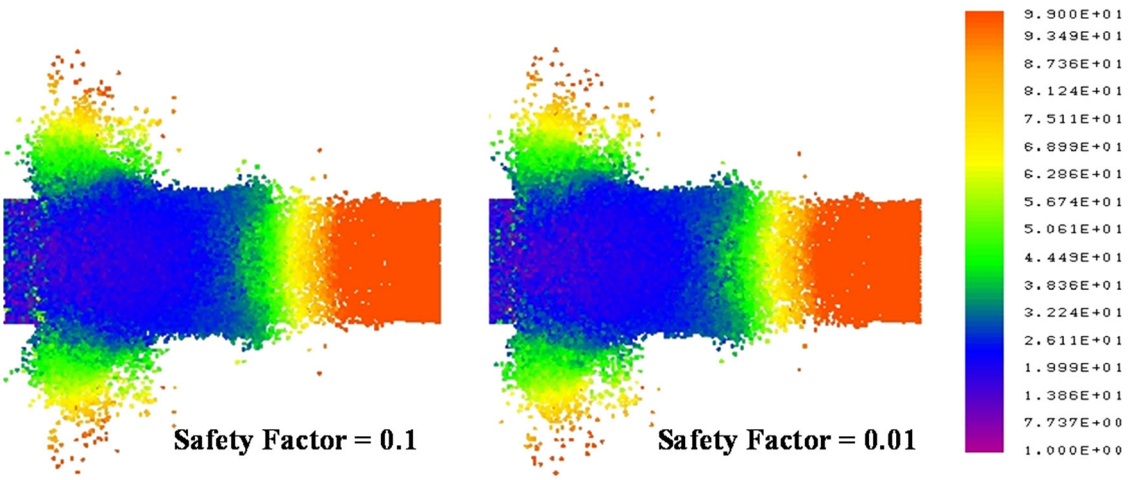

Fig. 17 Velocity magnitudes for 100-m/s impact at 250 μs

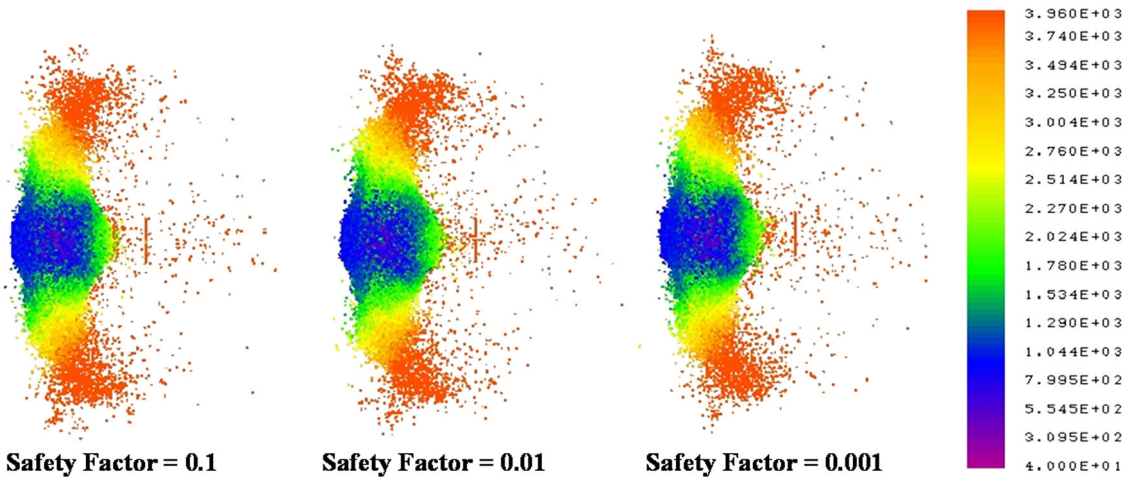

Fig. 18 Velocity magnitudes for 4000-m/s impact at 15 μs

7 Concluding remarks

A medium may be observed at various scales. In constructing a material model, a resolution level is selected. Below this level, details are not visible to the model and some enhancement to the model must be made to adequately capture, at least approximately, real phenomena. Nonlocality provides such an enhancement [25]. Peridynamics provides not only nonlocality, but also a consistent treatment of deformation and failure of a medium. Stochastic peridynamics provides, in addition, the capability to address spatial variability or lack of complete knowledge of properties of the medium.

In this paper, we provided a background of local and nonlocal continuum mechanics of random media in Sects. 3 and 4, and an approach to generalize peridynamics to random media in Sect. 5. We discussed a random media approach to many material systems, such as geological formations, where spatial variability or lack of complete knowledge of geometric or material properties leads to stochastic response under dynamic loading. One cannot do reliable simulations of impact, shock, and spalling such as shown in Sect. 6, without peridynamics. So, what we have accomplished is development of *computational stochastic peridynamics* via introduction of spatial random effects in such dynamics problems. The only way to proceed is by running large simulations, which we employed to study the parameter sensitivity.

To model spatial randomness of scalar properties other than mass density, bulk modulus, yield strength, or critical stretch, one may employ the same model as discussed here. For modeling vector or tensor properties, one can use tensor-valued random fields [26]. However, the crucial role in any realistic, random field model

is played by the mesoscale spatial resolution (L) chosen to represent the actual material. A larger value for L means weaker noise than seen at smaller values. In turn, a change in L affects the corresponding correlation structure [27]. Thus, for a specific choice of mesoscale L, one should determine the random field by the micromechanics upscaling as discussed here. Once this upscaling is done, one should investigate whether the spacing of peridynamic mesh roughly or exactly corresponds to the mesoscale. The closely related issue is whether the horizon should change when transitioning from peridynamics of a homogeneous medium to a randomly inhomogeneous medium.

Acknowledgments This research was made possible by the support from DTRA Grant HDTRA1-08-10-BRCWM and, in part, by the NSF under Grants CMMI-1462749 and IP-1362146 (I/UCRC on Novel High Voltage/Temperature Materials and Structures).

References

1. Grigoriu, M.: Stochastic Calculus, Applications in Science and Engineering. Birkhäuser, Boston (2002)
2. Soize, C.: Stochastic Models of Uncertainties in Computational Mechanics, Lecture Notes in Mechanics 2. ASCE (2012)
3. Ostoja-Starzewski, M.: Microstructural Randomness and Scaling in Mechanics of Materials. Chapman & Hall/CRC Press Inc, Boca Raton (2008)
4. Christakos, G.: Random Field Models in Earth Sciences. Dover, Mineola, NY (1992)
5. Porcu, E., Montero, J.M., Schlather, M.: Challenges in Space-Time Modelling of Natural Events. Springer, Berlin (2012)
6. Beran, M.: Statistical continuum mechanics: an Introduction. In: Jeulin, D., Ostoja-Starzewski, M. (eds.), Mechanics of Random and Multiscale Microstructures. CISM Courses and Lectures, vol. 430. Springer, New York (2000)
7. Hill, R.: Elastic properties of reinforced solids: some theoretical principles. J. Mech. Phys. Solids **11**, 357–372 (1963)
8. Mandel, J., Dantu, P.: Contribution à l'étude théorique et expérimentale du coefficient d'élasticité d'un milieu hétérogènes mais statisquement homogène. Annales des Ponts et Chaussées Paris **113**(2), 115–146 (1963)
9. Ranganathan, S., Ostoja-Starzewski, M.: Scaling function, anisotropy and the size of RVE in elastic random polycrystals. J. Mech. Phys. Solids **56**, 2773–2791 (2008)
10. Ostoja-Starzewski, M., Ranganathan, S.I.: Scaling and homogenization in spatially random composites. In: Mantic, V. (ed.) Chapter 2 in Mathematical Methods and Models in Composites, pp. 61–102. World Scientific, Singapore (2013)
11. Ostoja-Starzewski, M., Wang, X.: Stochastic finite elements as a bridge between random material microstructure and global response. Comp. Meth. Appl. Mech. Eng. **168**(1–4), 35–49 (1999)
12. Beran, M.J., McCoy, J.J.: Mean field variations in a statistical sample of heterogeneous linearly elastic solids. Int. J. Solids Struct. **6**, 1035–1054 (1970)
13. Beran, M.J., McCoy, J.J.: The use of strain gradient theory for analysis of random media. Int. J. Solids Struct. **6**, 1267–1275 (1970)
14. Silling, S.A.: Reformulation of elasticity theory for discontinuities and long-range forces. J. Mech. Phys. Solids **48**, 175–209 (2000)
15. Demmie, P.N., Silling, S.A.: An approach to modeling extreme loading of structures using peridynamics. J. Mech. Mater. Struct. **2**(10), 1921–1945 (2007)
16. Silling, S.A., Epton, M., Weckner, O., Xu, J., Askari, E.: Peridynamic states and constitutive modeling. J. Elast. **88**(2), 151–184 (2007)
17. Marsh, S.: LASL Shock Hugoniot Data. University of California Press, Berkeley (1980)
18. Ostoja-Starzewski, M., Sheng, P.Y., Jasiuk, I.: Influence of random geometry on effective properties and damage formation in 2-D composites. ASME J. Eng. Mater. Technol. **116**, 384–391 (1994)
19. Ostoja-Starzewski, M., Lee, J.D.: Damage maps of disordered composites: a Spring network approach. Int. J. Fract. **75**, R51–R57 (1996)
20. Alzebdeh, K., Al-Ostaz, A., Jasiuk, I., Ostoja-Starzewski, M.: Fracture of random matrix-inclusion composites: scale effects and statistics. Int. J. Solids Struct. **35**(19), 2537–2566 (1998)
21. Cooper, P.: Explosives Engineering. Wiley-VCH Inc, New York (1996)
22. URL for R statistical package is http://www.r-project.org/
23. Demmie, P.: Kraken User's Manual. SAND2011-5003, Sandia National Laboratories, Albuquerque, NM (2013)
24. Demmie, P.: Detonation modeling in peridynamic theory. In: Proceedings Fifteenth International Detonation Symposium, San Francisco, CA, Office of Naval Research publication number 43–280-15, July 2014
25. Jirásek, M.: Nonlocal theories in continuum mechanics. Acta Poly. **44**(5–6), 16–34 (2004)
26. Malyarenko, A., Ostoja-Starzewski, M.: Statistically isotropic tensor random fields: correlation structures. Math. Mech. Complex Syst. (MEMOCS) **2**(2), 209–231 (2014)
27. Sena, M., Ostoja-Starzewski, M., Costa, L.: Stiffness tensor random fields through upscaling of planar random materials. Probab. Eng. Mech. **34**, 131–156 (2013)